RSC Advances

PAPER

View Article Online
View Journal | View Issue

Cite this: *RSC Adv.*, 2023, **13**, 5557

Hollow nanotube arrays of nickle–cobalt metal sulfide for high energy density supercapacitors†

Ding Shen, [a] MingYue Li,[ab] Yaohan Liu,[a] Xiaofan Fu,[a] Haoran Yu,[a] Wei Dong *[a] and ShaoBin Yang*[a]

Received 30th November 2022
Accepted 8th February 2023

DOI: 10.1039/d2ra07624a

rsc.li/rsc-advances

High energy density is still difficult to achieve using existing metal sulfides because of their low specific capacitance. To improve capacitance, a series of nickel and cobalt metal sulfides with different Ni/Co ratios were synthesized by a two-step hydrothermal method. Using the combining method of experimental research and first-principles calculation, the morphology, structural stability, electronic structure and electrochemical properties of metal sulfides were investigated systematically. The results show that the morphology of metal sulfides gradually grows from two-dimensional structure to nanotube arrays, and finally to nanorod arrays, as the Ni/Co ratios decrease. Among them, the NC24 sample with the Ni/Co ratio of 1 : 2 is a hollow nanotube array composed of $NiCo_2S_4$, which shows excellent electrochemical performance. The specific capacity of the NC24 sample reaches 1527C g^{-1} at 1 A g^{-1}, and the capacity retention is 93.81% at 10 A g^{-1} after 2000 cycles. Furthermore, a symmetrical supercapacitor assembled from the $NiCo_2S_4$ nanotube array shows a high energy density of 67.5 W h kg^{-1}. This strategy develops a nanotube array of metal sulfides and expands its application in a high energy density supercapacitor.

1. Introduction

Due to the rapid development of society, the consumption of traditional fossil energy is huge and increasing gradually, which leads to a serious shortage of fossil energy and the aggravation of carbon dioxide pollution.[1–3] The development of new energy sources such as solar energy, wind energy and tidal energy is one of the main approaches to solve the above problem. However, these new energies can not be used directly on a large scale because of their randomness and instability. It is necessary to develop efficient energy conversion and storage devices.[4,5] As one of the energy storage devices, the supercapacitor has many advantages, such as high power density, fast charge and discharge speed, long cycle life, *etc.*, so supercapacitors and their electrode materials have been of wide concern for many researchers.[6–9]

However, the large-scale application of supercapacitor is seriously hindered by the low energy density, compared with batteries. The approach to improve the energy density of supercapacitor is to increase the specific capacitance and voltage window of electrode materials, according to the formula $E = 1/2CV^2$.[10] Therefore, electrode materials such as transition metal oxides, hydroxides and transition metal sulfides have become an important research field because of their high specific capacitance.[11,12] Transition metal sulfides have more flexible crystal structure and better electrical conductivity, compared with metal oxides and hydroxides.[13–15] Moreover, the valence range of Ni and Co in transition metal sulfides is wide, which is beneficial to the reversible redox reaction of nickle cobalt metal sulfides during the charge and discharge process.[16] Considering these characteristics, nickle–cobalt metal sulfides are considered to be one of the most promising electrode materials for supercapacitor.[17]

At present, many nickle–cobalt metal sulfides with various morphologies and nanostructures, such as zero-dimensional nanoparticles, one-dimensional nanotubes and nanorods, two-dimensional nanoflakes, three-dimensional sea urchins and flowers, *etc.*, are synthesized by chemical deposition, electrodeposition, solvothermal and sol–gel methods, respectively.

For example, Zhao *et al.*[18] prepared three-dimensional flaky $NiCo_xS_y$ materials by chemical deposition. The $NiCo_xS_y$ materials have rich mesoporous structure and good electrical conductivity, which is beneficial to improve their capacitance properties. Therefore, the specific capacitance of the $NiCo_xS_y$ materials is 1196 F g^{-1} when the current density is 1 A g^{-1} and the specific capacitance retention is 97.5% after 4000 cycles. When the current density increases to 20 A g^{-1}, the specific capacitance of the $NiCo_xS_y$ materials maintains 61.7% of the capacitance at 1 A g^{-1}, showing good structural stability and rate performance. Similarly, Shinde *et al.*[19] synthesized nanosheets-like $NiCo_2S_4$ materials by chemical deposition method. The nanosheets-like structure helps to improve the

[a]*College of Materials Science and Engineering, Liaoning Technical University, Fuxin, Liaoning 123000, China. E-mail: lgddongwei@163.com; lgdysb@163.com*

[b]*Institute of Engineering Technology and Natural Science, Belgorod State University, Belgorod 308015, Belgorod Oblast, Russia*

† Electronic supplementary information (ESI) available. See DOI: https://doi.org/10.1039/d2ra07624a

capacity of the electrode material, and the maximum capacitance can reach 1072 F g^{-1}. Shi *et al.*[20] prepared a three-dimensional hollow sea urchin-like $NiCo_2S_4$ material by solvothermal method. Due to the unique structure of both external sea urchin-like morphology and internal hollow structure, $NiCo_2S_4$ materials show high specific capacitance and rate performance. The specific capacitance of $NiCo_2S_4$ material is 1398 F g^{-1} at 1 A g^{-1}, and it still reaches 1110 F g^{-1} at 10 A g^{-1}. Tang *et al.*[21] prepared a three-dimensional flower-like $NiCo_2S_4$ material by first chemical precipitation and then annealing treatment. The crystal structure of the $NiCo_2S_4$ material modified by polyethylene glycol is pure and the specific surface area is larger, thus the electrochemical performance is significantly improved. The specific capacitance of the modified $NiCo_2S_4$ material is 2199 F g^{-1} at 1 A g^{-1}, and the specific capacitance retention is 82.0% after 1000 cycles at 10 A g^{-1}. Jiang *et al.*[22] prepared a three-dimensional pine cone structure Ni–Co–S_4 nanomaterial by a one-step solvothermal method. The specific capacitance of the Ni–Co–S_4 material is 2215 F g^{-1} at 0.5 A g^{-1}, and the specific capacitance retention is close to 90.2% after 10 000 cycles, showing good cycling performance. Wang *et al.*[23] successfully prepared a two-dimensional nanorod array $NiCo_2S_4$ material with a nanorod as the backbone and nanowires as the branch by using the hydrothermal method. The $NiCo_2S_4$ nanorod array has good electrochemical performance with a specific capacitance of 3093 F g^{-1} at 5 A g^{-1} and 2130 F g^{-1} at 30 A g^{-1}. In addition, the introduction of graphene,[24] carbon nanotubes,[25] graphite-like carbon nitride,[26] carbon fiber,[27] activated carbon[28] or polyaniline[29] into $NiCo_2S_4$ metal sulfides could also significantly improve the electrochemical performance, which have attracted wide attention.

The above results show that the structure and morphology of metal sulfide $NiCo_2S_4$ have a significant effect on its capacitance properties. However, it is impossible to directly compare and investigate the structure and morphology of $NiCo_2S_4$ material and their effects on electrochemical performance, due to different preparation methods or different synthesis conditions. Meanwhile, the interaction between Ni and Co in $NiCo_2S_4$ metal sulfides and the mechanism of improving the electrochemical performance have not been fully revealed, compared with Ni_3S_4 or Co_3S_4. In this paper, a series of nickle and cobalt metal sulfides were synthesized by a two-step hydrothermal method by adjusting the Ni/Co ratios and the effects of the Ni/Co ratios on the composition, morphology and capacitance properties of metal sulfides were investigated. Meanwhile, the formation energies of metal sulfides with different Ni/Co ratios and the electronic structures of typical metal sulfides, such as Ni_3S_4, $NiCo_2S_4$ and Co_3S_4, are calculated by the first principles.

2. Experimental and theoretical details

2.1. Synthesis of metal sulfides

A series of nickle–cobalt metal sulfides were synthesized by a two-step hydrothermal method, including the first synthesis of precursors and the second synthesis of nickle–cobalt metal sulphide by Na_2S. Firstly, seven groups of $NiCl_2 \cdot 6H_2O$ and $CoCl_2 \cdot 6H_2O$ were weighed, according to the molar ratio of Ni to Co of 6 : 0, 5 : 1, 4 : 2, 3 : 3, 2 : 4, 1 : 5 and 0 : 6, and then they were dissolved in deionized water of 40 mL, respectively. Then seven groups of 0.07 g urea were dissolved in 35 mL deionized water, respectively. The above two solutions were uniformly mixed and added into a Teflon-lined stainless steel autoclave. Then, the pre-cleaned nickle foam sheet (2.5 × 3 cm^2) was also put into the autoclave. The autoclave was kept at 120°C for 6 h, then cooled to room temperature. Then, the foamed nickle sheet with metal sulfide precursors was taken out and put into an ultrasonic cleaner for 2 min, then washed alternately with deionized water and ethanol many times.

The second step, seven groups of 0.72 g Na_2S were weighed and dissolved in deionized water of 75 mL, in which the Na_2S was used to sulfurize the precursors to prepare nickle–cobalt metal sulfides. And then put into the Teflon-lined stainless steel autoclave. The nickle foam sheet with metal sulfide precursors prepared in the previous step was put into the seven groups of an autoclave. These autoclaves were kept at 160°C for 6 h, and then cooled to room temperature. The nickle foam sheets with metal sulfides were taken out and washed alternately with deionized water and ethanol for many times. Finally, the metal sulfides with different Ni/Co ratios were obtained by drying at 60°C for 10 h, which were labeled as NC60, NC51, NC42, NC33, NC24, NC15 and NC06, respectively.

2.2. Characterization of morphology and structure

The phase analysis was carried out by powder X-ray diffractometer (XRD) with Cu tube, λ = 1.54182 nm (XRD-6100 Shimadzu). The morphological analysis was performed with the scanning electron microscope (SEM, JEOL 7600). The chemical properties and composition of the surface were measured by the X-ray photoelectron spectrometer (XPS, Thermo Fischer). The chemical states of cobalt, nickle and sulfur were measured by XPS with Al k_α radiation (1486.6 eV) and binding energies were calibrated by C 1s (284.6 eV). The high resolution images were tested by transmission electron microscope (TEM, Tecnai G2).

2.3. Characterization of electrochemical performance

The electrochemical performance of metal sulfides was carried out using an electrochemical workstation (CHI- 660E, Chenhua) in 6.0 mol L^{-1} KOH electrolyte. Using nickle foam loaded with metallic sulfides (~4.7 mg cm^{-2}) as working electrode, platinum plate as counter electrode and Hg/HgO electrode as reference electrode, a three-electrode system was assembled for the galvanostatic charge–discharge test, cyclic voltammetry test and AC impedance spectrum test. The specific capacitance (C_s), specific capacity (C) and theoretical specific capacity (C') of the electrode can be calculated by the following formula:[30]

$$C_s = I \times \Delta t/(m \times \Delta V) \quad (1)$$

$$C = I \times \Delta t/m \quad (2)$$

$$C' = nF/m \quad (3)$$

where C_s (F g^{-1}) is the specific capacitance, C (C g^{-1}) is the specific capacity, C' (C g^{-1}) is the theoretical specific capacity, I (A) is the discharge current, Δt (s) is the discharge time, m (g) is the mass of the active material, and ΔV (V) is the voltage window, n is the charges passed during faradaic redox reactions, F is the Faraday constant (96 485C mol^{-1}).

The cyclic voltammetry curve was tested in the voltage window of 0–0.54 V and the scanning rate of 2, 5, 10, 15, 20, 25, 30 and 50 mV s^{-1}, respectively. The AC impedance spectrum is measured with an AC amplitude of 5 mV and a frequency range of 10^{-2} to 10^5 Hz. Selecting a pair of foam nickle of loaded NC24 sample with excellent electrochemical performance as working electrodes, a symmetrical supercapacitor was assembled for energy density, power density and cycle life testing. The energy density (E) and power density (P) can be calculated by the formula (4):

$$E = C_{cell} \times \Delta V^2/7.2,\ P = 3600 \times E/\Delta t \quad (4)$$

where E (W h kg^{-1}) is the energy density, P (W kg^{-1}) is the power density, C_{cell} (F g^{-1}) is the specific capacitance, ΔV (V) is the voltage window, and Δt (s) is the discharge time. The cycle life test was carried out with 2000 charge–discharge at a current density of 10 A g^{-1}.

2.4. First-principles theoretical calculation

The formation energies of metal sulfides with different Ni/Co ratios and the electronic structures of typical metal sulfides, such as Ni_3S_4, $NiCo_2S_4$ and Co_3S_4, were calculated by CASTEP[31] based on density functional theory(DFT). In the process of calculation, the interaction between nuclei and valence electrons is described by Ultra-soft pseudopotential[32] and the electron exchange correlation can be carried out using PBE functional with generalized gradient approximation(GGA).[33] After testing, the energy cut-off for the plane-wave expansion is set to 500 eV, the atomic total energy convergence is set to 1.0×10^{-5} eV per atom, and the force convergence is set to 0.2 eV nm^{-1}. Due to the different crystal structures of metal sulfides, the Brillouin-zone integral is sampled by Monkhorst–Pack grid K points at an interval of about 0.02 $Å^{-1}$.[34]

In order to investigate the thermodynamic stability of metal sulfides, the formation energy (ΔE_f)[35] is defined as:

$$\Delta E_f = [E(Ni_xCo_yS_4) - xE(Ni) - yE(Co) - 4E(S)]/(x + y + 4) \quad (5)$$

where $E(Ni_xCo_yS_4)$, E(Ni), E(Co) and E(S) are the total energy of metal sulfides, the energies of simple substance Ni, Co and S respectively, x and y are the numbers of Ni and Co atoms in $Ni_xCo_yS_4$ molecular formula, respectively. When ΔE_f is negative, it shows that the structure of metal sulfides is thermodynamically stable, and the higher the absolute value of ΔE_f, the higher the structural stability of metal sulfides.

3. Results and discussion

3.1. Structural characterizations

In order to analyze the effect of the Ni/Co ratios on the structure of metal sulfides, all metal sulfides samples were analyzed by XRD and the results are shown in Fig. 1. From Fig. 1a, it can be found that the single nickle sulfide sample (NC60) has obvious diffraction peaks near 26.6, 31.4, 38.0, 50.1 and 54.7°. These diffraction peaks correspond to the standard JCPDS card of Ni_3S_4 (no. 08-0106), which indicates that the NC60 sample is mainly composed of cubic Ni_3S_4. Similarly, the diffraction peaks of a single cobalt sulfide sample (NC06) near 26.7, 31.7, 38.1, 47.5, 50.0 and 54.9°correspond to the standard JCPDS card of Co_3S_4 (no. 02-1361), which indicates that the NC06 sample is mainly composed of cubic phase Co_3S_4. For NC24 sample, the diffraction peaks appears at near 26.7, 31.5, 38.2, 50.3 and 55.2°, corresponding to the standard JCPDS card of $NiCo_2S_4$ (no. 43-1477). Therefore, combined with the XRD patterns of nickle–cobalt sulfides and the molar ratio of Ni and Co in the reactant raw materials, NC51 sample is composed of $NiCo_2S_4$ and Ni_3S_4, while NC33, NC24 and NC15 samples are composed of $NiCo_2S_4$ and Co_3S_4.

In order to investigate the thermodynamic structural stability of metal sulfides with different Ni/Co ratios, the formation energies (ΔE_f) of metal sulfides with different Ni/Co ratios are calculated by the first-principle calculation, and the results are shown in Fig. 1b. It can be seen from Fig. 1b that the value ΔE_f of metal sulfides with different Ni/Co ratios are all negative, indicating that these metal sulfides are thermodynamically stable. Among them, the value of ΔE_f of $NiCo_2S_4$ with space group $Fd\bar{3}m$ is the lowest, indicating that the thermodynamic structure of $NiCo_2S_4$ is the most stable. This also explains why the metal sulfides synthesized with different Ni/Co ratios are mainly composed of cubic $NiCo_2S_4$. The schematic of crystal structure of $NiCo_2S_4$ is shown in Fig. 1c. $NiCo_2S_4$ is cubic with space group $Fd\bar{3}m$, in which Co atoms are bonded with six equivalent S atoms to form a CoS_6 octahedron, and Ni atoms are bonded with four equivalent S atoms to form a NiS_4 tetrahedron.[36,37]

In order to further understand the electronic properties of metal sulfides, typical metal sulfides, such as Ni_3S_4, $NiCo_2S_4$ and Co_3S_4, were selected for structural optimization and electronic properties by first-principle calculation, and the

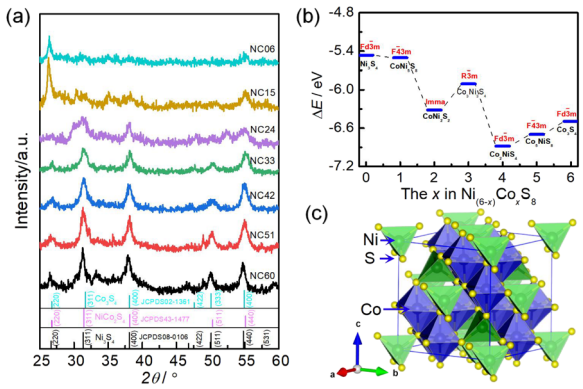

Fig. 1 Crystal structure and formation energy of metal sulfides with different Ni/Co ratios. (a) XRD patterns. (b) Formation energies. (c) Schematic of crystal structure for $NiCo_2S_4$ with the atoms occupying the Wyckoff positions: 8a, (0, 0, 0), for Co; 16d, (0.625, 0.625, 0.625), for Ni; and 32e (0.384, 0.384, 0.384), for S.

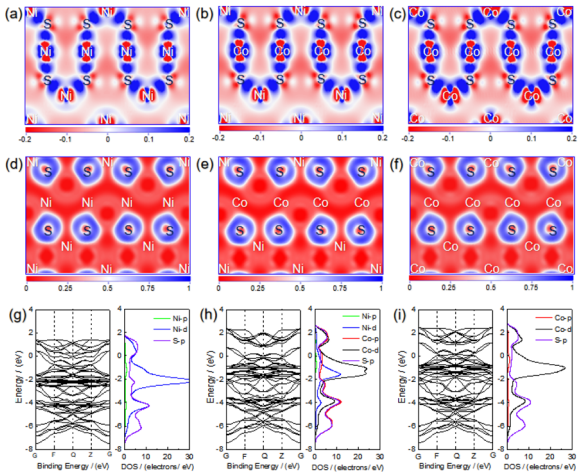

Fig. 2 The electronic structure of Ni_3S_4, $NiCo_2S_4$ and Co_3S_4. (a)–(c) Charge density difference for Ni_3S_4, $NiCo_2S_4$ and Co_3S_4, respectively. (d)–(f) Electronic local function for Ni_3S_4, $NiCo_2S_4$ and Co_3S_4, respectively. (g)–(i) Energy band and density of states for Ni_3S_4, $NiCo_2S_4$ and Co_3S_4, respectively.

results are shown in Fig. 2. Fig. 2a–c shows the charge density difference (CDF) of Ni_3S_4, $NiCo_2S_4$ and Co_3S_4. From Fig. 2a–c, it can be seen that the Ni or Co metal atoms lose electrons and the S atoms gain electrons, indicating that the electrons of Ni or Co metal atoms transfer to S atoms in Ni_3S_4, $NiCo_2S_4$ and Co_3S_4. Fig. 2d–f shows the electronic local function (ELF) of Ni_3S_4, $NiCo_2S_4$ and Co_3S_4, in which the value range of ELF is 0–1, as shown in the icon. As known, when the ELF value is 0.75–1, it is mainly a covalent bond, 0.5–0.75 is mainly a metal bond, and 0–0.5 is mainly a strong ionic bond. As can be seen from Fig. 2d–f, the Ni–S bond or Co–S bond in Ni_3S_4, $NiCo_2S_4$ and Co_3S_4 are all ionic bonds with certain covalent bond properties according the ELF value. Fig. 2g–i shows the energy band structure (EBS) and density of states (DOS) of Ni_3S_4, $NiCo_2S_4$ and Co_3S_4. From the EBS in Fig. 2g–i, it can be seen that Ni_3S_4, $NiCo_2S_4$ and Co_3S_4 all have electronic states near the Fermi level (0 eV), which shows that they all have good conductivity. The experimental results show that the electronic conductivity of $NiCo_2S_4$ is 1.25×10^6 S m^{-1} at room temperature,[38] which is in agreement with the theoretical calculation results. From the DOS near the Fermi level in Fig. 2g–i, it can be seen that the electronic state of Ni_3S_4 is mainly contributed by the electrons of Ni-3d and S-3p, while the electronic state of Co_3S_4 is mainly contributed by the electrons of Co-3d and S-3p, and the electronic states of $NiCo_2S_4$ are mainly contributed by electrons of Ni-3d, Co-3d, Co-4p and S-3p. The synergistic effect between Co and Ni in $NiCo_2S_4$ crystal leads to the change of electronic structure, especially the electrons transfer of Co-4p, which results in the shortening of Co–S bond from 0.226 nm in Co_3S_4 crystal to 0.214 nm, which indicates that the chemical bond of Co–S bond in $NiCo_2S_4$ crystal is shorter and the interaction is stronger. However, the change of Ni–S bond in $NiCo_2S_4$ crystal is not obvious compared with that in Ni_3S_4 crystal, which is between 0.219–0.220 nm.

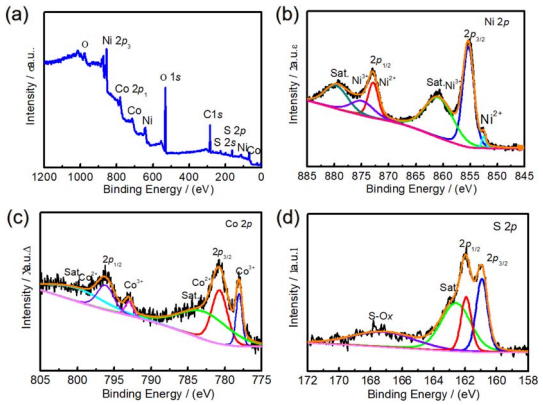

Fig. 3 XPS spectra of the NC24 sample. (a) Full spectrum. (b) High-resolution XPS spectra of Ni 2p. (c) High-resolution XPS spectra of Co 2p. (d) High-resolution XPS spectra of S 2p.

In order to analyze the elemental composition and valence distribution of NC24 samples in detail, the NC24 samples were analyzed by X-ray photoelectron spectra (XPS) and the results are shown in Fig. 3. As can be seen from Fig. 3a, the full spectra of NC24 sample shows that it contains Ni, Co, S, C and O elements, in which the molar ratio of Ni, Co and S is 0.96 : 1.84 : 4. That is to say, the chemical formula of NC24 sample is $Ni_{0.96}Co_{1.84}S_4$, which is close to its stoichiometric ratio of 1 : 2 : 4. It is also confirmed that the NC24 sample is composed of $NiCo_2S_4$, which is consistent with the results of XRD analysis in this paper. In addition, the O element may come from the slight oxidation on NC24 sample surface. Fig. 3b shows a high-resolution XPS spectra of Ni 2p. It can be seen from Fig. 3b that Ni $2p_{1/2}$ and Ni $2p_{3/2}$ are fitted by two peaks respectively, and the peaks of binding energy at 852.5 eV and 872.9 eV correspond to Ni^{2+}, binding energy at 855.3 eV and 874.9 eV belonged to Ni^{3+}, binding energy at 860.8 eV and 879.7 eV are satellite peaks, marked as "Sat." Fig. 3c is a high-resolution XPS spectra of Co 2p. Similarly, the peaks of binding energy at 780.7 eV and 796.2 eV correspond to Co^{2+}, binding energy at 778.1 eV and 793.0 eV belonged to Co^{3+}, binding energy at 782.8 eV and 800.1 eV are satellite peaks. The weak satellite peak indicates that most of the Co elements in NC24 sample exist in Co^{2+} state.[39] Fig. 3d is a high-resolution XPS spectra of S 2p, showing obvious main peaks and satellite peaks. The peaks of binding energy at 160.9 eV and 161.9 eV correspond to S $2p_{3/2}$ and S $2p_{1/2}$, respectively. The former is attributed to S^{2-} related to sulfur vacancy, and the latter to metal–sulfur bond (Ni–S and Co–S bond). The above results show that there are Ni^{2+}, Ni^{3+}, Co^{2+}, Co^{3+} and S^{2-} in the NC24 sample, which is consistent with the reports in the[40] literature.

3.2. Morphological characterizations

The effect of the Ni/Co ratios on the morphology of metal sulfides was observed by SEM and TEM, the typical morphology and structure of NC60, NC24 and NC06 are shown in Fig. 4 and the morphologies of other metal sulfides were observed by SEM as shown in the ESI Fig. S1,† the NC60 sample shows a two-

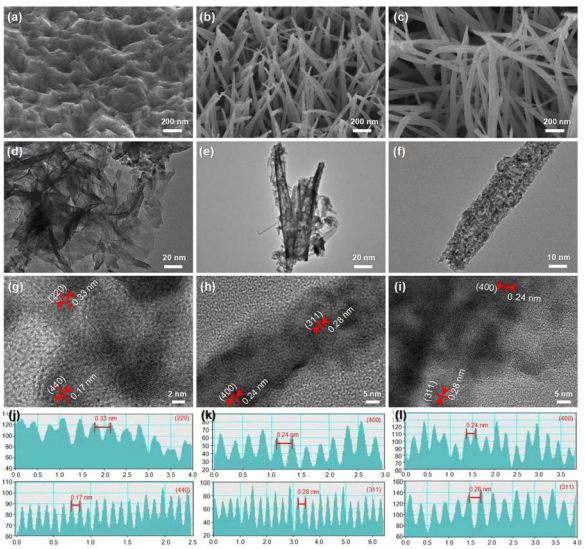

Fig. 4 The SEM images and TEM images of the NC60, NC24 and NC06 samples. (a) SEM image, (d) TEM image, (g) HRTEM image and (j) lattice and lattice spacing of the Fourier transform for the NC60 sample. (b) SEM image, (e) TEM image, (h) HRTEM image and (k) Lattice and lattice spacing of the Fourier transform for the NC24 sample. (c) SEM image, (f) TEM image (i) HRTEM image and (l) lattice and lattice spacing of the Fourier transform for the NC06 sample.

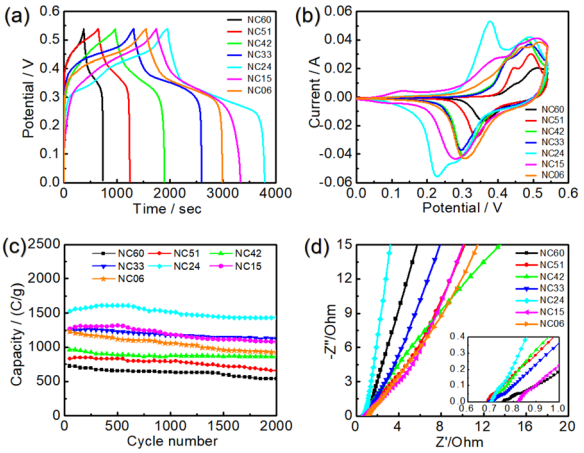

Fig. 5 The electrochemical performances of metal sulfides with different Ni/Co ratios. (a) Constant current charge–discharge curves of metal sulfides. (b) Cyclic voltammetry (CV) curves of metal sulfides at 2 mV s^{-1}. (c) Cycle performance curves of metal sulfides after 2000 cycles. (d) Electrochemical impedance spectra of metal sulfides.

dimensional uneven morphology. As the Ni/Co ratios decrease, the morphology of metal sulfides gradually grows from two-dimensional structure to nanotube arrays, in which NC24 samples have regular vertical morphology. When the Ni/Co ratio continues to decline, the nanotube arrays began to converge gradually for NC15 sample and the nanotube arrays grow into a nanorod arrays for NC06 sample, showing a messily intertwined morphology. This shows that the Ni/Co ratio has a significant effect on the morphology of nickle–cobalt metal sulfides.

It is found in Fig. 4d that the NC60 sample is a thin sheet composed of disordered flakes. The lattice spacing of 0.33 nm and 0.17 nm in the HRTEM image are consistent with the (220) and (440) planes of Ni_3S_4, respectively. As shown in Fig. 4e, the interior of the $NiCo_2S_4$ nanotube of NC24 samples is hollow, which provides a fast path for ion diffusion in the electrolyte. It is measured that the diameter of $NiCo_2S_4$ nanotubes is about 30 nm and the wall of the nanotubes is partially surrounded by thin nano flakes, which greatly increases the electroactive site. The lattice spacing of 0.28 nm and 0.24 nm belongs to the (311) and (400) planes of $NiCo_2S_4$, respectively. As shown in Fig. 4f, the NC06 sample shows a nanorod morphology and the lattice spacing of 0.28 nm and 0.24 nm corresponds to the (311) and (400) planes of Co_3S_4, respectively, which is consistent with the results of XRD analysis in Fig. 2.

3.3. Electrochemical performances

The electrochemical performances of metal sulfides with different Ni/Co ratios are shown in Fig. 5. According to formula (1), the specific capacities of NC60, NC51, NC42, NC33, NC24, NC15 and NC06 samples are calculated to be 721, 828, 964, 1244, 1527, 1270 and 1230C g^{-1}, respectively, from Fig. 5a. This shows that specific capacity of the NC06 sample is higher than that of NC60 samples. Meanwhile, with the decrease of Ni/Co ratio, the specific capacity of metal sulfides increased at first and then decreased, in which the specific capacity of NC24 sample composed mainly of $NiCo_2S_4$ reached the maximum value of 1527C g^{-1}.

Fig. 5b shows the cyclic voltammetry (CV) curves of metal sulfides. There are obvious redox peaks in these cyclic voltammetry curves, which indicates that all metal sulfides undergo redox reactions during the charge and discharge process. This is due to the change of the valence of Ni^{2+}/Ni^{3+}, Co^{2+}/Co^{3+} and Co^{3+}/Co^{4+} in the metal sulfides electrode materials, which belongs to pseudo-capacitance characteristics.[41]

Cycle performance is an important parameter to evaluate the electrochemical performance of supercapacitor. Fig. 5c shows the cycle performance curve of metal sulfides at the current density of 1 A g^{-1}. After 2000 cycles, the samples of NC60, NC51, NC42, NC33, NC24, NC15 and NC06 maintained 74.12%, 79.17%, 89.08%, 90.60%, 93.81%, 85.30% and 75.30% of the first specific capacity, respectively. This shows that the structural stability and cycle performance of NC24 samples mainly composed of $NiCo_2S_4$ are the best. In particular, the specific capacity of the NC24 sample increases gradually before 500 cycles, and begins to decline gradually after 500 cycles. This change phenomenon also exists in Ni–Co–P material for supercapacitors,[42] which may be due to the fact that the infiltration and diffusion of electrolyte is a time-consuming process before all the electrochemical activities of electrode materials can be excited.

The measured electrochemical impedance spectra are shown in Fig. 5d, in which a slanted line at low frequency and a semicircle at high frequency region. It can be seen from Fig. 5d that the equivalent series resistance R_s intercept of curve on the x-axis[43] of the NC51, NC42, NC33 and NC24 samples are 0.68–0.71

Ω, lower than that of other samples. Furthermore, the NC24 sample shows the maximum linear slope at low frequency, which showing a good diffusion behavior of ion in the electrode material. This may be related to the fact that the $NiCo_2S_4$ material with hollow nano-array is beneficial to the diffusion of the electrolyte.

Because of the excellent electrochemical performance of NC24 samples composed of $NiCo_2S_4$, the constant current charge–discharge tests of NC24 samples were carried out at a current density of 1, 2, 5, 10, 15, 20 and 30 A g^{-1}, respectively. The relationship between the current density and specific capacity is shown in Fig. 6a. As can be seen from Fig. 6a, the specific capacity values of NC24 samples at different current densities are 1527, 1485, 1428, 1327, 1244, 1154 and 982C g^{-1}, respectively, which indicates that NC24 samples have good rate performance, and the specific capacity at the current density of 30 A g^{-1} maintains 64.36% of the specific capacity at the current density of 1 A g^{-1}.

In order to further investigate the charge storage mechanism of NC24 sample, the cyclic voltammetry curves of NC24 sample were measured in the range of 2–30 mV s^{-1} and the results are shown in Fig. 6b. At a lower scanning rate of 2 mV s^{-1}, a pair of significant redox peaks are observed near 0.37 and 0.22 V, which indicates that the specific capacity is mainly attributed to the following typical reaction process:[44,45]

$$NiCo_2S_4 + OH^- + H_2O \leftrightarrow NiS_{(4-4x)}OH + 2CoS_{2x}OH + e^- \quad (6)$$

$$CoS_{2x}OH + OH^- \leftrightarrow CoS_{2x}O + H_2O + e^- \quad (7)$$

$$CoS_{2x} + OH^- \leftrightarrow CoS_{2x}OH + e^- \quad (8)$$

$$NiS_{(4-4x)} + OH^- \leftrightarrow NiS_{(4-4x)}OH + e^- \quad (9)$$

With the increase of scanning rate, the oxidation peak and reduction peak move to higher potential and lower potential, respectively.

According to the electrochemical reaction mechanism of electrode materials,[46–48] the rapid reversible electrochemical reactions occur in the redox pairs of Ni^{2+}/Ni^{3+}, Co^{2+}/Co^{3+} and Co^{3+}/Co^{4+} during the charging process of $NiCo_2S_4$. So nickel and cobalt ions in $NiCo_2S_4$ can be turned into an oxidation state of +4. Considering the total charges passed is 4 mol per 1 mol $NiCo_2S_4$, the calculated theoretical pesudocapacitance of $NiCo_2S_4$ is 1267C g^{-1}, according to the theoretical capacitance calculation formula (3). It should be mentioned that the capacity of the N24 sample has exceeded the theoretical capacity of $NiCo_2S_4$, which may be caused by the synergistic effect of pseudo-capacitance and electric double-layer capacitance formed by hollow structure.[49,50]

The relationship between the different scanning rates (v) and the current density (i) at reduction peak is obtained from Fig. 6b, as shown in Fig. 6c. And the charge–discharge mechanism can be qualitatively evaluated by the formula:

$$i = aV^b \quad (10)$$

where a and b are adjustable constants. Usually, the diffusion control is dominant in the charge–discharge process when b is 0.5 and the surface control plays a dominant role when b is 1.[51,52] The b value of the fitting result is 0.57 ± 0.05, which is between 0.5 and 1. The results show that the redox process of NC24 samples composed of $NiCo_2S_4$ is controlled by both diffusion and surface capacitance.

Fig. 6d further shows the contribution rates of diffusion and surface capacitance in the redox process of $NiCo_2S_4$ at different scanning speeds. With the increase of scanning rate, the ion diffusion contribution of redox reaction of $NiCo_2S_4$ electrode increases, which shows that metal sulfides have some electrochemical properties of the battery.[53]

There are two important indexes to evaluate the application prospect of supercapacitors, namely, energy density and power density. Under the current density of 10 A g^{-1} and the window voltage of 1.5 V, the specific capacitance of the symmetrical supercapacitor assembled by $NiCo_2S_4$ electrode is 176.7 F g^{-1}. Therefore, according to formula (3), the symmetrical supercapacitor device shows a high energy density of 67.5 W h kg^{-1} at a power density of 795.3 W kg^{-1}. These values are higher than those reported in the existing literature about $NiCo_2S_4$ metal sulfides and their composites for supercapacitors, as shown in Table 1.

Above all, a series of nickle–cobalt metal sulfides were synthesized by a two-step hydrothermal method and the Ni/Co ratios of nickel–cobalt metal sulfides has an important influence on the morphology, composition and structure, as well as their electrochemical properties. The NC60 and NC06 samples is composed of single phase Ni_3S_4 and Co_3S_4, respectively. The NC24 sample is composed of $NiCo_2S_4$, and other samples are two-phase mixtures. Among them, the NC24 sample composed of $NiCo_2S_4$ has excellent electrochemical performance. This is due to the fact that the metal sulfide $NiCo_2S_4$ with hollow nanotube arrays has rapid ion diffusion properties, which is confirmed by AC impedance spectroscopy. The above results demonstrate that the assembled symmetrical devices have a promising applications for high energy density supercapacitor.

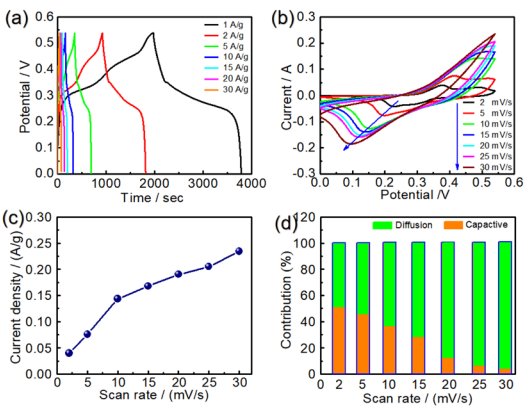

Fig. 6 The electrochemical performances of the NC24 sample. (a) Constant current charge–discharge curves. (b) Cyclic voltammetry (CV) curves. (c) Relationship between scanning rates and the current density. (d) Contribution rates of diffusion and surface capacitance.

Table 1 Capacitance properties of nickle–cobalt sulfides and their composites with different morphology

Materials	Morphology	Specific capacitance	Cycling performance	Energy density	Ref.
$NiCo_xS_y$	Flaky	1196 F g^{-1} at 1 A g^{-1}	97.5% after 4000 cycles	—	18
$NiCo_2S_4$	Urchin-like hollow	1398 F g^{-1} at 1 A g^{-1}	74.4% after 5000 cycles	39.3 W h kg^{-1} at 749.6 W kg^{-1}	20
$NiCo_2S_4$	Flower-like	2199 F g^{-1} at 1 A g^{-1}	80.0% after 3000 cycles	38.2 W h kg^{-1} at 400.0 W kg^{-1}	21
Ni–Co–S_4	Pine cone	2215 F g^{-1} at 1 A g^{-1}	90.2% after 10 000 cycles	36.6 W h kg^{-1} at 850.0 W kg^{-1}	22
$NiCo_2S_4$	Nanorod array	3093 F g^{-1} at 5 A g^{-1}	41.7% after 2000 cycles	39.3 W h kg^{-1} at 800.0 W kg^{-1}	23
$NiCo_2S_4$/DG	Nanosheet	1137 F g^{-1} at 2 A g^{-1}	7.1% after 5000 cycles	25.6 W h kg^{-1} at 8000.0 W kg^{-1}	54
$NiCo_2S_4$/3DGF	Nanowire array	1455 F g^{-1} at 1.3 A g^{-1}	96.0% after 3000 cycles	—	55
$NiCo_2S_4$@NiS/CoS	Nanoflake	2551 F g^{-1} at 2 A g^{-1}	86.4% after 10 000 cycles	58.4 W h kg^{-1} at 8002.4 W kg^{-1}	56
$NiCo_2S_4$/PANI/CNTs	Hierarchy	1290 mF cm^{-2} at 2 mA cm^{-2}	80.1% after 5000 cycles	83.3 μW h cm^{-2} at 420 μW cm^{-2}	57
$NiCo_2S_4$	Hollow nanotube array	1527C g^{-1} at 1 A g^{-1}	93.8% after 2000 cycles	67.5 W h kg^{-1} at 795.3 W kg^{-1}	This work

4. Conclusions

In brief, a series of nickle–cobalt metal sulfides with different Ni/Co ratios were synthesized by a two-step hydrothermal method. The experimental results show that nickle–cobalt metal sulfides are mainly composed of $NiCo_2S_4$, which can be confirmed by the conclusion that $NiCo_2S_4$ phase is the most stable in thermodynamics calculated by the first principle. Furthermore, the synergistic effect between Co and Ni in $NiCo_2S_4$ phase leads to the change of electronic structure and makes the Co–S bond stronger. As the Ni/Co ratios decrease, the morphology of metal sulfides gradually grows from two-dimensional structure to nanotube arrays, and finally to nanorod arrays. Among them, the NC24 sample with the Ni/Co ratio of 1 : 2 is $NiCo_2S_4$ hollow nanotube array, showing excellent electrochemical performance. The specific capacity of the $NiCo_2S_4$ nanotube array is as high as 1527C g^{-1} at 1 A g^{-1} and the specific capacity maintained 93.81% of the initial capacity after 2000 cycles at 10 A g^{-1}. The symmetrical supercapacitor assembled by the $NiCo_2S_4$ nanotube array show a high energy density of 67.5 W h kg^{-1}. Thus, the reported strategies may attract widespread interest in the research electrode materials for high energy density supercapacitor.

Author contributions

Conceptualization, Shen D.; methodology, Yang S. B.; and Dong W., investigation, Li M. Y.; data curation, Liu Y. H.; writing—original draft preparation, Fu X. F.; writing—review and editing, Yu H. R.; project administration, All authors have read and agreed to the published version of the manuscript.

Conflicts of interest

There are no conflicts to declare.

Acknowledgements

Financial supports from the National Natural Science Foundation of China (Grant No. 51874167, 21808095, 51774175), China Postdoctoral Science Foundation Funded Project (2018M641707), Discipline Innovation Team of Liaoning Technical University (LNTU20TD-09) are greatly acknowledged.

References

1 X. Chu, F. Meng, T. Deng, Y. Lu, O. Bondarchuk, M. Sui, M. Feng, H. Li and W. Zhang, *Nanoscale*, 2020, **12**, 5669–5677.
2 H. Huang, Y. Tang, L. Xu, S. Tang and Y. Du, *ACS Appl. Mater. Interfaces*, 2014, **6**, 10248–10257.
3 S. Wang, Z. Xiao, S. Zhai, G. Wang, W. Niu, L. Qin and Q. An, *Electrochim. Acta*, 2020, **343**, 136106.
4 J. Wang, X. Zhang, Z. Li, Y. Ma and L. Ma, *J. Power Sources*, 2020, **451**, 227794.
5 Y. Tian, H. Huang, G. Liu, R. Bi and L. Zhang, *Chem. Commun.*, 2019, **55**, 3243–3246.
6 S. Wang, Z. Xiao, S. Zhai, G. Wang, Q. An and D. Yang, *Electrochim. Acta*, 2019, **309**, 197–208.
7 X. Zhang, A. Wu, X. Wang, C. Tian, R. An and H. Fu, *J. Mater. Chem. A*, 2018, **6**, 17905–17914.
8 M. Gao, W. K. Wang, X. Zhang, J. Jiang and H. Q. Yu, *J. Phys. Chem. C*, 2018, **122**, 25174–25182.
9 R. Zhao, D. Cui, J. Dai, J. Xiang and F. Wu, *Sustainable Mater. Technol.*, 2020, **24**, 00151.
10 W. Zhao, Y. Zhu, L. Zhang, Y. Xie and X. Ye, *J. Alloys Compd.*, 2019, **787**, 1–8.
11 W. He, C. Wang, H. Li, X. Deng, X. Xu and T. Zhai, *Adv. Energy Mater.*, 2017, **7**, 1700983.
12 Z. Peng, L. Gong, J. Huang, Y. Wang, L. Tan and Y. Chen, *Carbon*, 2019, **153**, 531–538.
13 W. Yang, R. Zhao, J. Xiang, S. Loy, Y. Di, J. Li, M. Li, D. Ma and F. Wu, *J. Colloid Interface Sci.*, 2022, **626**, 866–878.
14 D. Zha, Y. Fu, L. Zhang, J. Zhu and X. Wang, *J. Power Sources*, 2018, **378**, 31–39.
15 X. Yu, M. Wang, A. Gagnoud, Y. Fautrelle, Z. Ren and X. Li, *Mater. Des*, 2018, **145**, 135–143.
16 Y. Y. Chen, P. Dhaiveegan, M. Michalska and J. Y. Lin, *Electrochim. Acta*, 2018, **274**, 208–216.
17 C. Liu and X. Wu, *Mater. Res. Bull.*, 2018, **103**, 55–62.
18 F. Zhao, W. Huang and D. Zhou, *J. Alloys Compd.*, 2018, **755**, 15–23.
19 S. K. Shinde, M. B. Jalak, G. S. Ghodake, N. C. Maile, V. S. Kumbhar, D. S. Lee, V. J. Fulari and D. Y. Kim, *Appl. Surf. Sci.*, 2019, **466**, 822–829.
20 Z. Shi, X. Shen, Z. Zhang, X. Wang, N. Gao, Z. Xu, X. Chen and X. Liu, *J. Colloid Interface Sci.*, 2021, **604**, 292–300.

21 J. Tang, W. Huang, X. Lv and Q. Shi, *Nanotechnology*, 2020, **32**, 085604.
22 J. Jiang, Y. Sun, Y. Chen, X. Hu, L. Zhu, H. Chen and S. Han, *Mater. Sci.*, 2019, **54**, 11936–11950.
23 S. Wang, P. Zhang and C. Liu, *Colloids Surf., A*, 2021, **616**, 126334.
24 J. Xiao, H. Tong, F. Jin, D. Gong, X. Chen, Y. Wu, Y. Zhou, L. Shen and X. Zhang, *J. Power Sources*, 2022, **518**, 230763.
25 H. Chen, X. Ma and P. K. Shen, *Chem. Eng. J.*, 2019, **364**, 167–176.
26 R. Peymanfar and S. Ghorbanian-Gezaforodi, *Nanotechnology*, 2020, **31**, 495202.
27 X. Xiong, G. Waller, D. Ding, D. Chen, B. Rainwater, B. Zhao, Z. Wang and M. Liu, *Nano Energy*, 2015, **16**, 71–80.
28 M. M. Baig and I. H. Gul, *J. Energy Storage*, 2021, **37**, 102477.
29 Y. Wang, J. Zhong, F. Ding, Q. Zhao, Z. Zhang, X. Liu, Y. Liu, H. Rao, P. Zou and X. Wang, *New J. Chem.*, 2018, **42**, 9398–9409.
30 K. Xu, W. Li, Q. Liu, B. Li, X. Liu, L. An, Z. Chen, R. Zou and J. Hu, *J. Mater. Chem. A*, 2014, **2**, 4795–4802.
31 S. J. Clark, M. D. Segall, C. J. Pickard, P. J. Hasnip, M. J. Probert, K. Refson and M. Payne, *Z. Kristallogr. - Cryst. Mater.*, 2005, **220**, 567–570.
32 D. Vanderbilt, *Phys. Rev. B: Condens. Matter Mater. Phys.*, 1990, **41**, 7892–7895.
33 J. P. Perdew, K. Burke and M. Ernzerhof, *Phys. Rev. Lett.*, 1996, **77**, 3865.
34 Y. Pan, Y. Wang, M. Ye, R. Qu, H. Zhong, Z. Song, X. Peng, D. Yu, J. Yang, J. Shi and J. Lu, *Chem. Mater.*, 2016, **28**, 2100–2109.
35 X. Shi, S. L. Bernasek and A. Selloni, *J. Phys. Chem. C*, 2016, **120**, 14892–14898.
36 Y. Gao and K. Huang, *Chem.–Asian J.*, 2017, **12**, 1969–1984.
37 M. Dakshana and S. Meyvel, *Vacuum*, 2021, **192**, 110499.
38 C. Xia, P. Li, A. N. Gandi, U. Schwingenschlögl and H. N. Alshareef, *Chem. Mater.*, 2015, **27**, 6482–6485.
39 H. Wan, J. Jiang, J. Yu, K. Xu, L. Miao, L. Zhang, H. Chen and Y. Ruan, *CrystEngComm*, 2013, **15**, 7649–7651.
40 Y. Liu, J. Zhang, S. Wang, K. Wang, Z. Chen and Q. Xu, *New J. Chem.*, 2014, **38**, 4045–4048.
41 Y. Ruan, J. Jiang, H. Wan, X. Ji, L. Miao, L. Peng, B. Zhang, L. Lv and J. Liu, *J. Power Sources*, 2016, **301**, 122–130.
42 X. Zhang, A. Wu, X. Wang, C. Tian, R. An and H. Fu, *J. Mater. Chem. A*, 2018, **6**, 17905–17914.
43 L. Mei, T. Yang, C. Xu, M. Zhang, L. Chen, Q. Li and T. Wang, *Nano Energy*, 2014, **3**, 36–45.
44 T. Liu, Y. Zheng, W. Zhao, L. Cui and J. Liu, *J. Colloid Interface Sci.*, 2019, **556**, 743–752.
45 J. Zhao, Y. Wang, Y. Qian, H. Jin, X. Tang, Z. Huang, L. Lou, Q. Zhang, Y. Lei and S. Wang, *Adv. Funct. Mater.*, 2023, **33**, 2210238.
46 J. Yan, L. Mao, H. Duan, D. Zhu, Y. Lv, L. Li, L. Gan and M. Liu, *Chin. Chem. Lett.*, 2022, **33**, 2681–2686.
47 X. Zheng, L. Mao, Z. Song, W. Du, D. Zhu, Y. Lv, L. Li, L. Gan and M. Liu, *J. Mater. Chem. A*, 2022, **10**, 611–621.
48 Z. Song, L. Mao, l. Ruhimann, Y. Lv, D. Zhu, L. Li, L. Gan and M. Liu, *Adv. Funct. Mater.*, 2022, **32**, 2208049.
49 X. Yu, M. Wang, A. Gagnoud, Y. Fautrelle, Z. Ren and X. Li, *Mater. Des.*, 2018, **145**, 135–143.
50 G. Xiang, Y. Meng, G. Qu, J. Yin, B. Teng, Q. Wei and X. Xu, *Sci. Bull.*, 2020, **65**, 443–451.
51 F. Lu, M. Zhou, W. Li, Q. Weng, C. Li, Y. Xue, X. Jiang, X. Zeng, Y. Bando and D. Golberg, *Nano Energy*, 2016, **26**, 313–323.
52 M. K. Sahoo and G. Rao, *Electrochim. Acta*, 2018, **268**, 139–149.
53 H. Xuan, Y. Guan, X. Han, X. Liang, Z. Xie, P. Han and Y. Wu, *Electrochim. Acta*, 2020, **335**, 135691.
54 C. Jing, X. Guo, L. Xia, Y. Chen, X. Wang, X. Liu, B. Dong, F. Dong, S. Li and Y. Zhang, *Chem. Eng. J.*, 2019, **379**, 122305.
55 Z. Kang, Y. Li, Y. Yu, Q. Liao, Z. Zhang, H. Guo, S. Zhang, J. Wu, H. Si, X. Zhang and Y. Zhang, *J. Mater. Sci.*, 2018, **53**, 10292–10301.
56 Y. Chen, L. Wang, H. Gan, Y. Jiang, J. Feng, J. Liu and X. Shi, *J. Energy Storage*, 2022, **47**, 103626.
57 X. Cheng, D. Wang, H. Ke, Y. Li, Y. Cai and Q. Wei, *Comp. Commun.*, 2022, **30**, 101073.